Chapter 4

Photon-photon coupling induced transparency and absorption

In the previous two chapters we have focused on the effects of nonlinearity on transmission through an array of direct and side coupled qubits. In the rest of the thesis the focus is on exotic effects due to dissipative coupling in hybrid quantum systems. In this chapter we study a linear analogue of the nonlinear electromagnetically induced transparency (EIT) and electromagnetically induced absorption (EIA) phenomena, which we name coupling induced transparency (CIT) and coupling induced absorption (CIA) respectively. The effects are achieved via normal and dissipative coupling among the modes. We have developed a comprehensive quantum model capturing both these phenomena and also performed high frequency electromagnetic simulation of suitable devices for observing these quantum effects.

4.1 Theoretical formalism

To engineer the observation of CIT and CIA for any two interacting modes, we propose a general theoretical model for a hybrid quantum system as schematically shown in Fig. 4.1. It comprises of two resonating modes A and B, positioned on either side of a common signal line through which both modes are being driven. Both modes, mode A and B are coupled to the signal line and also coupled with each other through a complex coupling constant.

4.1.1 Hamiltonian for two modes and signal line

The general Hamiltonian for the system involving coherent and dissipative couplings in a two-mode system having common signal line can be written as [Tiwari et al., 2024; Rao

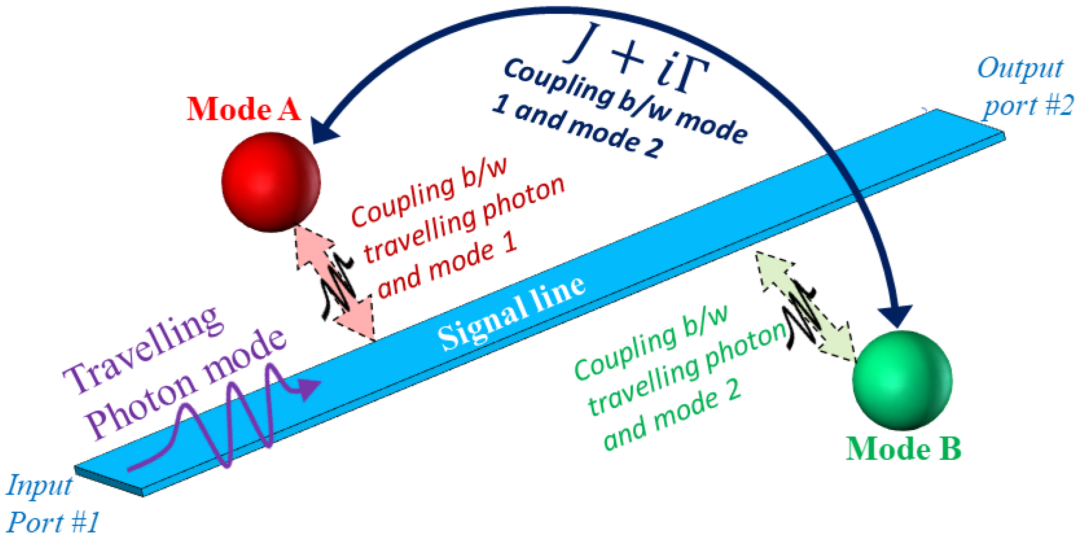

Fig. 4.1 Schematic diagram showing two modes A and B with a common signal line and different attributes of the system.

et al., 2020; Harder et al., 2021]

$$H/\hbar = (\omega_A - i\alpha)\hat{A}^\dagger\hat{A} + (\omega_B - i\beta)\hat{B}^\dagger\hat{B} + \Delta(\hat{A}\hat{B}^\dagger + \hat{A}^\dagger\hat{B}) + \int \omega_k \hat{p}_k^\dagger \hat{p}_k \, dk$$
$$+ \int [\lambda_A(\hat{A} + \hat{A}^\dagger)(\hat{p}_k + \hat{p}_k^\dagger) + \lambda_B(\hat{B} + \hat{B}^\dagger)(\hat{p}_k + \hat{p}_k^\dagger)]dk \tag{4.1}$$

Here $\hat{A}(\hat{A}^\dagger)$ and $\hat{B}(\hat{B}^\dagger)$ are the annihilation (creation) operators of the modes A and B respectively. ω_A and ω_B denote the resonance frequencies of the uncoupled modes A and B respectively, while α and β denote the intrinsic damping rates of these two modes respectively, $\Delta = J + i\Gamma$ where J and Γ are real parameters that characterize the strength of coherent and dissipative interactions between the two modes.

The fourth term in the Hamiltonian represents the signal line connected to the input and output ports. In our Hamiltonian formulation, we have modelled it as traveling photons, integrating over a real domain from $-\infty$ to $+\infty$. $\hat{p_k}^\dagger(\hat{p_k})$ is bosonic creation (annihilation) operator of the traveling photon obeying $\left[\hat{p}_k, \hat{p}_{k'}^\dagger\right] = \delta(k - k')$. The frequency of the travelling photon is denoted by ω_k where k represents the wave vector. The fifth term accounts for the interaction between each mode and traveling photons, modelled linearly in $\hat{p}_k^\dagger$ and $\hat{p}_k$. Each mode, A and B, exhibits a distinct coupling strength λ_A and λ_B respectively, arising from the interaction of traveling photons with modes A and B, respectively.

4.1.2 Heisenberg-Langevin Equations

Following the rotating-wave approximation (RWA) and solving Eq. 4.1, the equation of motion for $\hat{p_k}$ (travelling photon) can be written as [Tiwari et al., 2024; Rao et al., 2020; Harder et al., 2021; Walls and Milburn, 2008; Scully and Zubairy, 1997a]

$$\dot{\hat{p}}_k = \frac{-i}{\hbar}[\hat{p}_k, H] = -i\omega_k \hat{p}_k - i\lambda_A \hat{A} - i\lambda_B \hat{B} \tag{4.2}$$

This can be solved to give a time forwarded equation for the travelling wave operator, where the initial time $t_0 < t$ and $\hat{p_k}(t_0)$ is the initial state of the operator

$$\hat{p}_k(t) = e^{-i\omega_k(t-t_0)}\hat{p}_k(t_0) - \int_{t_0}^{t} i\left[\lambda_A \hat{A} + \lambda_B \hat{B}\right] e^{-i\omega_k(t-t')} dt' \tag{4.3}$$

The input field operator at the input port is defined as

$$\hat{p}_{in}(t) = \frac{1}{\sqrt{2\pi}} \int e^{-i\omega_k(t-t_0)}\hat{p}_k(t_0) dk \tag{4.4}$$

The equation for mode A operator is

$$\dot{\hat{A}} = \frac{-i}{\hbar}\left[\hat{A}, H\right] = -i\tilde{\omega}_A \hat{A} - \int i\lambda_A \hat{P}_k dk - i\Delta\hat{B} \tag{4.5}$$

By incorporating Eq. 4.3 and 4.4 in Eq. 4.5, the time forwarded Heisenberg-Langevin equation of the coupled system becomes

$$\dot{\hat{A}}(t) = -i\tilde{\omega}_A \hat{A}(t) - i\sqrt{\gamma}\hat{P}_{in}(t) - \gamma\hat{A}(t) - \sqrt{\kappa\gamma}\hat{B}(t) - i\Delta\hat{B}(t) \tag{4.6}$$

Similarly, for the mode B we get

$$\dot{\hat{B}}(t) = -i\tilde{\omega}_B \hat{B}(t) - i\sqrt{\kappa}\hat{P}_{in}(t) - \kappa\hat{B}(t) - \sqrt{\kappa\gamma}\hat{A}(t) - i\Delta\hat{A}(t) \tag{4.7}$$

where $\tilde{\omega}_A = \omega_A - i\alpha$ and $\tilde{\omega}_B = \omega_B - i\beta$. $\gamma = 2\pi\lambda_A^2$ and $\kappa = 2\pi\lambda_B^2$ represent the extrinsic damping rates of the mode A and B respectively. The steady state equations in the frequency domain can be obtained by applying a Fourier transformation to Eqs. 4.6 and 4.7, yielding [Tiwari et al., 2024; Rao et al., 2020]

$$i(\omega - \tilde{\omega}_A)\hat{A}(\omega) - i\sqrt{\gamma}\hat{P}_{in}(\omega) - \gamma\hat{A}(\omega) - \sqrt{\kappa\gamma}\hat{B}(\omega) - i\Delta\hat{B}(\omega) = 0 \tag{4.8}$$

$$i(\omega-\tilde{\omega_B})\hat{B}(\omega)-i\sqrt{\kappa}\hat{P}_{in}(\omega)-\kappa\hat{B}(\omega)-\sqrt{\kappa\gamma}\hat{A}(\omega)-i\Delta\hat{A}(\omega)=0 \tag{4.9}$$

Further we can write the time retarded equation for the travelling wave operator from Eq. 4.2, with reference to a later time $t_1 > t$

$$\hat{p}_k(t)=e^{-i\omega_k(t-t_1)}\hat{p}_k(t_1)+\int_t^{t_1} i[\lambda_A\hat{A}+\lambda_B\hat{B}]e^{-i\omega_k(t-t')}dt' \tag{4.10}$$

The output field operator at output port is defined as

$$\hat{p}_{out}(t)=\frac{1}{\sqrt{2\pi}}\int e^{-i\omega_k(t-t_1)}\hat{p}_k(t_1)dk \tag{4.11}$$

Using Eq. 4.10 and 4.11 in Eq. 4.5 the time retarded Heisenberg-Langevin equations of the coupled system in the time and frequency domains are

$$\dot{\hat{A}}(t)=-i\tilde{\omega_A}\hat{A}(t)-i\sqrt{\gamma}\hat{P}_{out}(t)+\gamma\hat{A}(t)+\sqrt{\kappa\gamma}\hat{B}(t)-i\Delta\hat{B}(t) \tag{4.12}$$

$$\dot{\hat{B}}(t)=-i\tilde{\omega_B}\hat{B}(t)-i\sqrt{\kappa}\hat{P}_{out}(t)+\kappa\hat{B}(t)+\sqrt{\kappa\gamma}\hat{A}(t)-i\Delta\hat{A}(t) \tag{4.13}$$

$$i(\omega-\tilde{\omega_A})\hat{A}(\omega)-i\sqrt{\gamma}\hat{P}_{out}(\omega)+\gamma\hat{A}(\omega)+\sqrt{\kappa\gamma}\hat{B}(\omega)-i\Delta\hat{B}(\omega)=0 \tag{4.14}$$

$$i(\omega-\tilde{\omega_B})\hat{B}(\omega)-i\sqrt{\kappa}\hat{P}_{out}(\omega)+\kappa\hat{B}(\omega)+\sqrt{\kappa\gamma}\hat{A}(\omega)-i\Delta\hat{A}(\omega)=0 \tag{4.15}$$

4.1.3 Transmission

Either solving Eq. 4.8 and 4.14 or Eq. 4.9 and 4.15 we can get the relation between input and output fields as

$$\hat{P}_{out}=\hat{P}_{in}-2i\sqrt{\kappa}\hat{B}(\omega)-2i\sqrt{\gamma}\hat{A}(\omega) \tag{4.16}$$

We can solve Eq. 4.8 and 4.9 to get the field operators in terms of the input field as

$$\hat{A}(\omega)=\frac{\hat{P}_{in}(\Delta\sqrt{\kappa}+i\beta\sqrt{\gamma}+\sqrt{\gamma}\omega-\sqrt{\gamma}\omega_B)}{(i\Delta+\sqrt{\kappa\gamma})^2+(i\alpha+i\gamma+\omega-\omega_A)(i\beta+i\kappa+\omega-\omega_B)} \tag{4.17}$$

$$\hat{B}(\omega) = \frac{\hat{P}_{in}(\Delta\sqrt{\gamma} + i\alpha\sqrt{\kappa} + \sqrt{\kappa}\omega - \sqrt{\kappa}\omega_A)}{(i\Delta + \sqrt{\kappa\gamma})^2 + (i\alpha + i\gamma + \omega - \omega_A)(i\beta + i\kappa + \omega - \omega_B)} \tag{4.18}$$

The experimentally measurable and numerically simulated parameter for these kinds of experiments is the transmission coefficient S_{21} between ports 1 and 2 of the hybrid system, which for our geometry gives

$$S_{21} = \frac{\hat{p}_{out}}{\hat{p}_{in}} - 1 \tag{4.19}$$

Utilizing Eq. 4.16, 4.17 and 4.18 in Eq. 4.19 yields the S_{21} as follows

$$S_{21} = \frac{2\alpha\kappa + 2\beta\gamma - 4i\Delta\sqrt{\kappa\gamma} - 2i\gamma(\omega - \omega_B) - 2i\kappa(\omega - \omega_A)}{(i\Delta + \sqrt{\kappa\gamma})^2 + (i\alpha + i\gamma + \omega - \omega_A)(i\beta + i\kappa + \omega - \omega_B)} \tag{4.20}$$

We will begin by examining the conditions under which the CIT and CIA phenomena manifest, each of which will be exemplified by the notions of LR and LA, respectively. We use extrinsic damping constants for the mode A, $\gamma = 0.01$, and mode B, $\kappa = 0.001, 0.0001$ which are consistent with experimental values of hybrid systems [Bhoi et al., 2022; Bernier et al., 2018; Hu et al., 2022; Rao et al., 2020; Harder et al., 2021]. The resonance frequencies of mode A and B are $\omega_A = 4.22$ GHz and $\omega_B = 3.84$ to 4.59 GHz with intrinsic damping $\alpha = 0.001$, and $\beta = 0.001$ respectively [Bhoi et al., 2022; Bernier et al., 2018; Hu et al., 2022; Rao et al., 2020; Harder et al., 2021]. The coupling constant is $J + i\Gamma^{'}$, where $\Gamma^{'} = \Gamma + \sqrt{\gamma\kappa}$. Using Eq. 4.20, we numerically calculate the $|S_{21}|$ power on the $\omega_r - \omega$ plane for the two different conditions; (i) $J \gg \Gamma^{'}$ and (ii) $\Gamma^{'} \gg J$. Under the dominance of J (i.e. $J \gg \Gamma^{'}$), a normal anticrossing dispersion pattern (CIT) emerges, revealing two higher and lower coupled branches around the resonant frequencies of modes A and B, indicative of the robust coherent coupling between them [see Fig. 4.2(a)]. On the other hand, for case of dominating $\Gamma^{'}$ (i.e. $\Gamma^{'} \gg J$), a contrasting shape of anticrossing dispersion (i.e., CIA) is observed, as shown in Fig. 4.2(c). Quite recently, such opposite anticrossing dispersion was also demonstrated, but in complex hybrid systems at a very low temperature below 50 mK [Zheng et al., 2023; Li et al., 2022].

To understand the similarity and difference of such CIT and CIA dispersion shapes that depends on the coherent and dissipative interactions between the modes A and B, a coupling matrix is constructed as given by,

$$H_{coupling} = \begin{pmatrix} \tilde{\omega}_{A'} & \Delta^{'} \\ \Delta^{'} & \tilde{\omega}_{B'} \end{pmatrix} \tag{4.21}$$

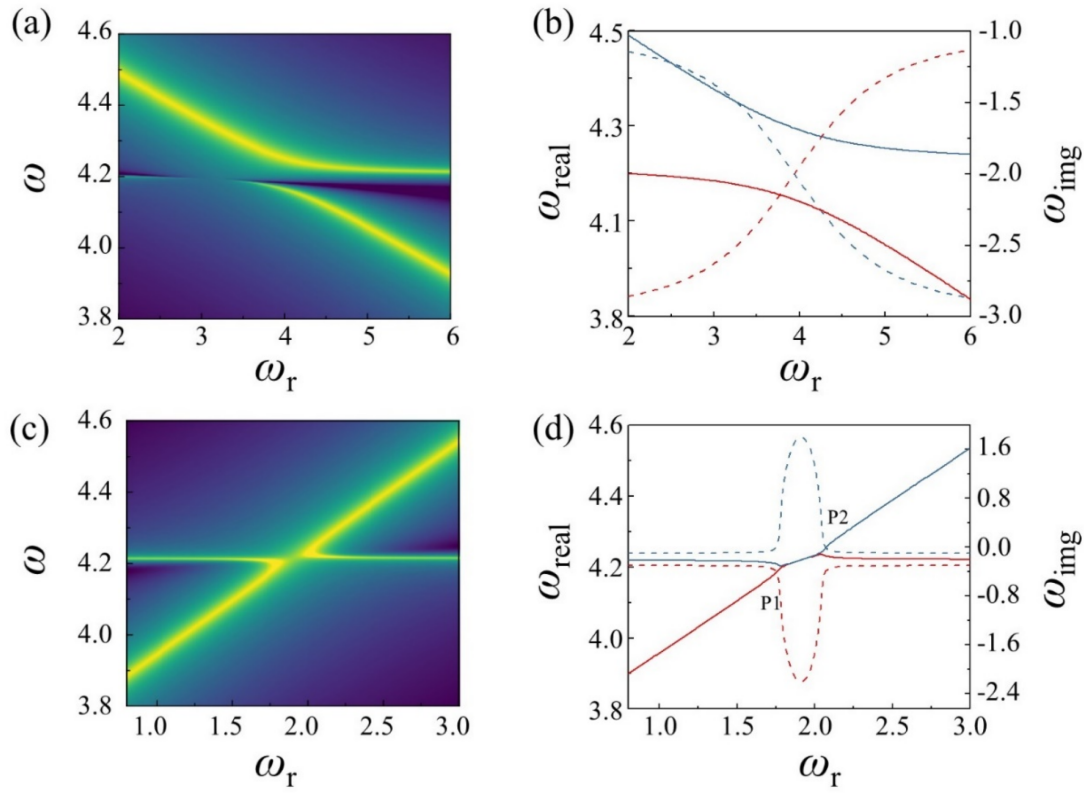

Fig. 4.2 Theoretical calculations of dispersion spectra (a) for case-1 $(J > \Gamma)$ and (c) for case-2 $(\Gamma > J)$. Theoretical calculations of resonance frequencies (solid lines) and linewidths (dotted lines) (b) for case-1 $(J > \Gamma)$ and (d) for case-2 $(\Gamma > J)$.

where $\tilde{\omega}_{A'} = \omega_A - i\alpha'$ and $\tilde{\omega}_{B'} = \omega_B - i\beta'$ with $\alpha' = (\alpha + \gamma)$ and $\beta' = (\beta + \kappa)$. The effective coupling constant $\Delta' = J + i\Gamma'$ with $\Gamma' = \Gamma + \sqrt{\gamma\kappa}$. Eq. 4.21 can be written as

$$H_{coupling} = \frac{\tilde{\omega}_{A'} + \tilde{\omega}_{B'}}{2}\mathbb{I} + \frac{\omega_A - \omega_B}{2}\sigma_z + J\sigma_x - i\frac{\alpha' - \beta'}{2}\sigma_z + i\Gamma'\sigma_x \tag{4.22}$$

where $\mathbb{I}$ is an identity matrix and σ_x , σ_z are Pauli matrices. The term proportional to the identity just causes a shift in the complex eigenvalues. In a system with a Hermitian coupling matrix, normal anticrossing or level repulsion (LR) is observed, while in the case of a purely anti-Hermitian matrix, opposite anticrossing or level attraction (LA) occurs [Bernier et al., 2018; Metelmann and Clerk, 2014]. So, we can express the coupling matrix in the general form $C\sigma_c + iD\sigma_d$, with real coefficients C and D. In this general form, level repulsion (attraction) occurs when the Pauli matrix with a dominating real (imaginary) coefficient is present [Bernier et al., 2018; Metelmann and Clerk, 2014]. When other parameters are held constant, a dominant real coefficient, particularly when $J \gg \Gamma'$, leads to LR, whereas reversing this condition results in LA. From the eigenvalue analysis of the coupling matrix, we get higher (lower) branches of eigenfrequency given by

$$E_{\pm} = \frac{\tilde{\omega}_{A'} + \tilde{\omega}_{B'} \pm \sqrt{4(\Delta')^2 + (\tilde{\omega}_{A'} - \tilde{\omega}_{B'})^2}}{2} \tag{4.23}$$

Using this equation, we have numerically calculated the complex eigenvalues of two coupled modes, i.e., $E_{\pm} = \omega_{real} \pm i\omega_{img}$, where ω_{real} and ω_{img} represent the dispersion shape and the linewidth evolution of the coupled modes, respectively.

For two specific cases of $J \gg \Gamma'$ and $\Gamma' \gg J$, the resultant theoretical calculations are given in Figs. 4.2(b) and 4.2(d), respectively. For the case of dominating J, the dispersion shape (real value ω_{real}) of E_+ and E_- branches repel each other [Fig. 4.2(b)], while their linewidths (imaginary value ω_{img}) of E_+ and E_- cross each other [Fig. 4.2(b)]. This behaviour is ubiquitous in any coupled systems involving reciprocal energy transfers as reported in references [Bhoi et al., 2022; Rao et al., 2021b; Zheng et al., 2023; Bernier et al., 2018; Li et al., 2022]. It has been observed in a multimode optomechanical circuit with dissipation engineering [Bernier et al., 2018], between magnon mode of two YIG spheres mediated by cavity photon of a superconducting resonators [Li et al., 2022]. On the other hand, for the case of dominating Γ' , the dispersion shape (ω_{real}) of E_+ and E_- provide the energies of their states that attract each other and nearly meet at two points [denoted as P1 and P2 in Fig. 4.2(d)], while their linewidth (imaginary value ω_{img}) of E_+ and E_- are found to be repulsive (they do not cross each other), as shown in the Fig. 4.2(d). Such LA has been studied in a 3D microwave cavity using an YIG sphere [Harder et al., 2021], between

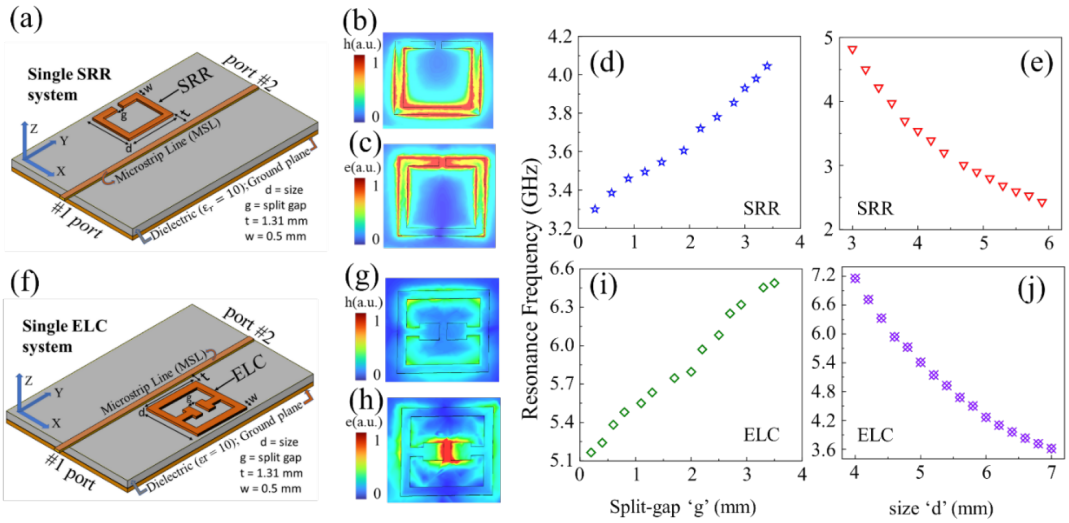

Fig. 4.3 Schematic diagram of planar resonators loaded microstripline for numerical simulation (a) split ring resonator (SRR) and (f) electric inductive-capacitive resonator (ELC). Electric and magnetic fields distributions for SRR and ELC are shown in (b, c) and (g, h) respectively. Dependence of resonance frequency on split gap size (d, i) and resonator size (e, j) for (d, e) SRR and (i, j) ELC.

magnon mode of two YIG spheres mediated by propagating photons of a coplanar waveguide [Li et al., 2022].

4.2 Resonator design and numerical simulation set up

To develop the devices showing the observed effects, we employed the electromagnetic full-wave solver CST Microwave Studio to design and conduct numerical simulations on a planar hybrid system comprising two photon resonators. Among the two resonators, one is a split-ring resonator (SRR) while the other is an electric inductive-capacitive resonator (ELC), as schematically shown in Fig. 4.3(a) and Fig. 4.3(f), respectively. In the microstrip line configuration, electric fields emanate from the central strip, terminating perpendicular to the ground plane, while a microwave magnetic field form around the microstrip line. The resonators were positioned in close proximity to the microstrip line, allowing them to be excited by the induced currents from the transverse microwave magnetic field when microwave currents flow through the microstrip feeding line. In this state, the resonators function as a parallel LC resonant circuit, resulting in a quasi-static resonant effect.

4.2.1 Numerical simulation of individual SRR and ELC

Before considering the hybrid system, we investigate the fine tunability in the resonance frequency for both the SRR and ELC by adjusting their dimensions. The microstrip line was designed to have a width $w = 0.64\ mm$, a length $l = 50\ mm$, and a thickness $t = 35\ \mu m$ in order to have a 50Ω characteristic impedance. The planar substrate (Gray colour in Fig. 4.3) had dimensions of 50 *mm*, 25 *mm*, and 0.64 *mm*, a relative permittivity of 10, and a dissipation factor of 0.0012 at 10 GHz. The SRR is configured with dimensions of $d = 5\ mm$, and $g = 0.4\ mm$, as illustrated in Fig. 4.3(a). By keeping the other geometrical parameters of the SRR constant, we conduct numerical simulation systematically varying the split gap 'g' from 0.3 to 3.4 *mm*. This results in an increase in the resonance frequency from 3.3 GHz to 4.05 GHz as 'g' varies between 0.3 and 3.4 *mm* as shown in Fig. 4.3(d). On the other hand, the resonance frequency decreases from 4.82 GHz to 2.43 GHz as the size of the SRR changes from 3 to 5.9 *mm* for a fixed value of 'g' = 0.4 *mm* (Fig. 4.3 (e)). Similarly, a separate simulation is performed for the ELC with geometrical parameters of $d = 5\ mm$, and $g = 0.2$ to 3.5 *mm*, as indicated in Fig. 4.3(f). Like SRR, its resonance frequency increases from 5.2 GHz to 6.5 GHz as 'g' is varied between 0.2 and 3.5 *mm* (for fixed $d = 5\ mm$), but decreases from 7.2 GHz to 3.6 GHz as 'd' changes from 4 to 7 *mm* (for fixed g = 0.4 *mm*) as shown in Fig. 4.3(i) and 4.3(j) respectively. These variations in resonance frequency with geometrical parameters can be well understood by viewing the resonators as basic LC circuits, with a resonance frequency $\omega = \frac{1}{2\pi}\sqrt{LC}$, where the inductance (L) and capacitance (C) arise from the conducting path and the split gaps of the resonators respectively. As the split gap widens, the capacitance ($C = \varepsilon A/g$) decreases, leading to an increase in the resonance frequency of the resonators. Conversely, increasing the dimensions of the resonators extends the conducting path, resulting in a decrease in the resonance frequency of the resonators. This relationship between the geometrical parameters and the resonant response provides a guide to design the compact planar photon-photon hybrid system based on the transmission lines loaded with SRR and ELC.

4.2.2 Numerical simulation of SRR/ELC hybrid system

In order to understand and uncover the intricate dynamic interactions between two photon modes, we design SRR and ELC in a single hybrid system by closely placing them on either side of the microstripline as shown in Fig. 4.4(a). When an ac current of microwave frequency is transmitted through the microstripline, a substantial portion of the microwave magnetic field lines generated by the microstrip is anticipated to permeate both the SRR and ELC, resulting in a strong electrodynamic coupling between them. This interaction between the

photon modes of the SRR and ELC facilitates an energy exchange through their overlapping electric and magnetic fields. This leads to the hybridization of resonance modes, which can be observed in phenomena such as mode splitting by analysing the intensity distribution.

The changes in resonators' electric and magnetic fields, driven by factors like geometry, orientation, position, and electromagnetic properties, impact the constructive or destructive interference that affects the electromagnetic coupling of SRR and ELC. Therefore, the simulation is conducted for two cases: For case-1 the SRR split gap is fixed (at $g = 0.6\,mm$), while SRR size 'd' varies from $2 \times 2\ mm^2$ to $6 \times 6\ mm^2$. For case-2, SRR size is fixed ($d = 4 \times 4\ mm^2$) while the split gap 'g' varies from 0.8 to 3.2 mm. The other dimensions such as outer dimension ($5 \times 5\ mm^2$), and split gap (0.2 mm) and size of ELC resonator are fixed for all cases.

4.3 Coupling between SRR's and ELC's photon modes

We record the transmission parameter (S_{21}) of the coupled SRR-ELC hybrid system as a function of the microwave frequency f of the ac current flowing in the microstrip line for different values of SRR's size and SRR's split gap representing case-1 and case-2 respectively. Fig. 4.4 (b) shows the $|S_{21}|$ spectra of SRR-ELC hybrid system under simulation conditions corresponding to case -1, revealing the presence of two distinct peaks. One peak (marked by red arrows) is very strongly dependent on the SRR's size and continuously shifts towards the lower-frequency side with increasing unit size, and crosses the other peak position (blue arrows), thus indicating the SRR's photon mode. The other peak does not move much, thus indicating the ELC mode. It is worth noting that as one peak approaches the other, there is a gradual change in their amplitudes. The maximum change occurs precisely as one peak crosses over the other, after which they gradually return to their original magnitudes.

Similarly, the interaction between SRR and ELC for case-2 is shown in Fig. 4.4 (c). As the SRR split gap increases, the SRR mode approaches the ELC mode and combines into a unified mode at the coupling center, resulting in an increase in amplitude. Continued widening of the SRR split gap causes the unified mode to separate into two distinct peaks of SRR and ELC. The shifts in resonance frequency positions and amplitudes depicted in Fig. 4.4(b) and (c) demonstrate a robust electrodynamics interaction between the SRR and ELC photon modes in the hybrid system. However, a noteworthy observation is that as the SRR size increases (case-1), the peaks approach each other but never coalesce into a single peak. Instead, they exhibit a transparency region at the coupling center, indicating a distinct level repulsion or CIT phenomenon. On the other hand, increase in SRR split gap

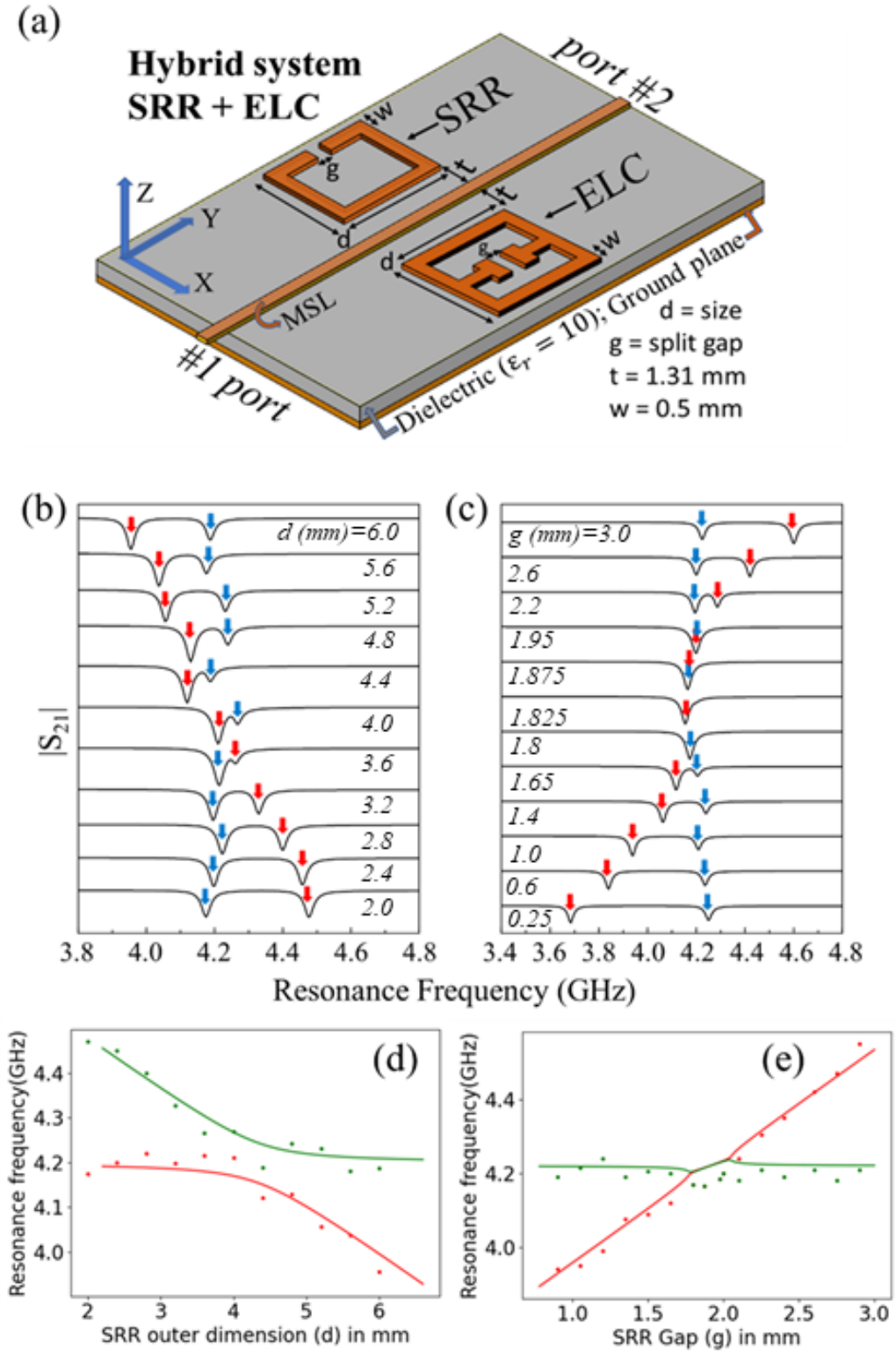

Fig. 4.4 (a) Schematic drawing of planar hybrid system comprising of SRR and ELC. $|S_{21}|$ spectra of SRR-ELC hybrid sample as function of (b) SRR size and (c) SRR split gap. Frequencies of the resonance peaks from (b, c) as functions of (d) SRR size and (e) SRR split gap. Dots: simulation data; solid lines: Theoretically fitted with Eq. 4.23.

(case-2), resulted, a merging of two modes into a single mode indicating level attraction or CIA phenomenon.

In order to examine the coupling effect, we extract the resonance frequency values from the $|S_{21}|$ spectra and plot a graph illustrating the relationship between the SRR geometrical parameter and the corresponding hybrid resonance frequencies in Fig. 4.4 (d, e). This graphical representation allows us to observe how changes in the SRR size / split gap influence the resonant behaviour of the coupled SRR-ELC system. In order to understand such contrasting anticrossing effects observed for the case-1 and case-2 geometries, we estimate the coupling constant by fitting with Eq. 4.23 to the lower- and higher-frequency branches (solid lines) of the coupled modes. From the fitting we obtained the numerical values of coupling constant $J = 0.075$ and $\Gamma^{'}$=0.02 MHz for the CIT [Fig. 4.4(d)] and the CIA [Fig. 4.4(e)], respectively. The simulated results are well fitted with Eq. 4.23 obtained from our theoretical modelling. We note that for the CIA, we obtain only the imaginary value of $\Delta^{'}$, whereas for the CIT, the real value of $\Delta^{'}$. Therefore, the real and imaginary values for $\Delta^{'}$ characterize the CIT and the CIA phenomena, respectively. According to Eq. 4.23, the real and imaginary numbers of $\Delta^{'}$ are the cases of J dominating and $\Gamma^{'}$ dominating respectively.

4.4 Transition between CIT and CIA

In order to understand the effect of various controlling parameters determining the contrasting dispersions during photon-photon interactions and the transitions between CIT and CIA, we further analyse the general coupling matrix with all dissipation and coupling terms present. From Eq. 4.23 we can write

$$E_+ - E_- = \sqrt{4(\Delta^{'})^2 + (\tilde{\omega}_{A^{'}} - \tilde{\omega}_{B^{'}})^2} \tag{4.24}$$

For level attraction the real (imaginary) part of eigenfrequencies should (should not) cross each other. In other words, the real part of $E_+ - E_-$ is zero for some input frequency, while its imaginary part will never be zero. At the crossing of the real part, we get $(E_+ - E_-)^2_{imaginary\ part} = 0$ and $(E_+ - E_-)^2_{real\ part} < 0$. Solving together gives,

$$|J| < \frac{|\alpha^{'} - \beta^{'}|}{2} \tag{4.25}$$

$$\Gamma^{'} = \frac{(\alpha^{'} - \beta^{'})(\omega_A - \omega_B)}{4J} \tag{4.26}$$

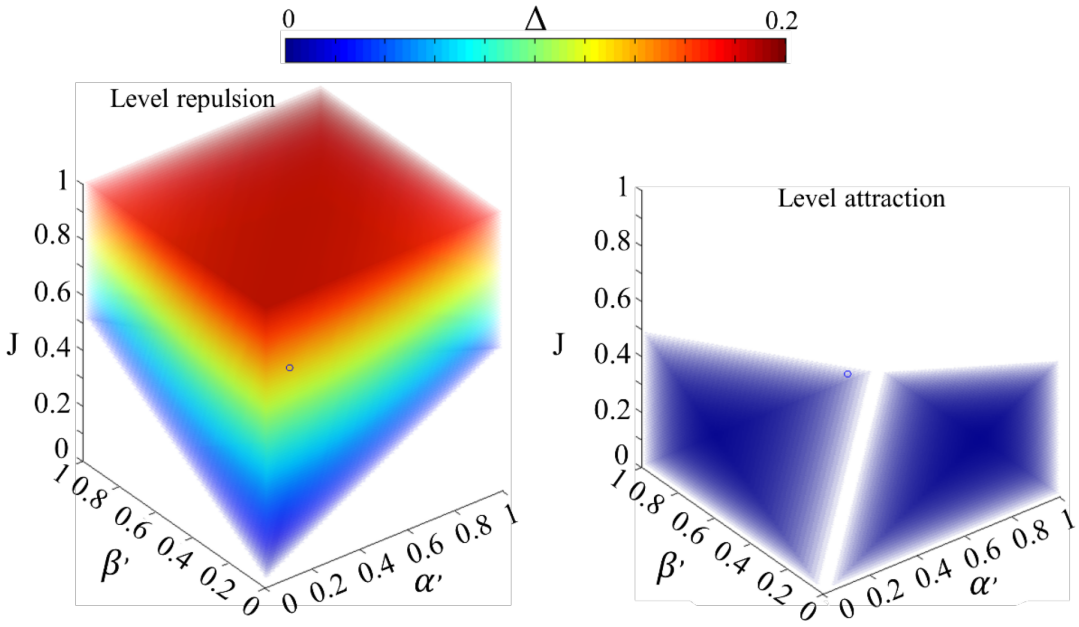

Fig. 4.5 Phase diagrams of CIT and CIA for total dissipation for both the modes and J while keeping $\Gamma = 0$. (a) level repulsion i.e. CIT and (b) level attraction i.e. CIA.

Thus, to observe level attraction, the coherent coupling (J) should be small while the dissipative coupling ($\Gamma^{'}$) should be large. To explore the effect of damping of each mode and how that is dominating the level attraction and level repulsion phenomenon, and how their interplay is affected by other parameters we have plotted 3D colour map for the different range of parameters. Our final result depends on four variables $\alpha^{'}$, $\beta^{'}$, J and $\Gamma^{'}$ apart from the resonator's eigenfrequencies which we keep fixed. We consider two specific cases (case-1 and case-2) for varying J and $\Gamma^{'}$.

Fig. 4.5 represents a pictorial overview of different possibilities of the coupling Hamiltonian in terms of $\alpha^{'}$, $\beta^{'}$, J and $\Gamma^{'}$ as variable. For case-1 Fig. 4.5(a) and (b) shows the 3D colourmap where we have taken, $\Gamma^{'} = 0.001$, and have plotted the real part of the difference of the eigenvalues for different values of $\alpha^{'}$, $\beta^{'}$ and J. Fig. 4.5 (a) shows the region of level repulsion which violates Eq. 4.25. We clearly see that J is dominating for the level repulsion. Fig. 4.5(b) shows the region of level attraction which is complementary to that of level repulsion. We observe from Fig. 4.5(b) that for $\Gamma^{'}$=0.001, there is a large region of level attraction at $J = 0$ which decreases gradually as J is increased. This region is symmetric about the $\alpha^{'} = \beta^{'}$ line. This decrease continues till $J = 0.05$ above which there is only level repulsion. The parameters of the hybrid system we considered for case-1 is a

point ($J = 0.075$, $\alpha^{'} = 0.011$ and $\beta^{'} = 0.0011$) shown in the 3D colourmaps which is inside the Fig. 4.5(a) but outside the Fig. 4.5(b). As mentioned before the two figures Fig. 4.5(a) and Fig. 4.5(b) are complementary to each other and their boundary have may also have exceptional points which have gained significant interest lately in exploring the topological nature of coupled hybrid systems [Bernier et al., 2018; Harder et al., 2017].

4.5 Conclusion

We have established a comprehensive theoretical framework for the observation of CIT and CIA in a coupled hybrid system, which is verified through numerical device simulation for photon-photon interaction in a planar SRR-ELC hybrid system. The dominant coherent and dissipative interaction between the photon modes leads to CIT and CIA respectively. Theoretical quantum calculations, in excellent agreement with full device simulations, reveal the physical origins of various interactions, enabling substantial control over both coupling strength and a controllable transition between CIT and CIA through manipulation of the dissipation rates of the two modes. Our theoretical model combined with numerical simulations and theoretical calculations, can contribute to understanding the physics of coupled systems and investigating interactions among excitations such as plasmons, magnons, and phonons, which are valuable for quantum information processing. Moreover, this work can open several theoretical and experimental endeavors to explore similar phenomena that potentially help in the advancement of concepts important for the development of quantum photonic and nonreciprocal quantum devices.